micromachines

Communication

Analytical and Physical Investigation on Source Resistance in $In_xGa_{1-x}As$ Quantum-Well High-Electron-Mobility Transistors

Ji-Hoon Yoo [1], In-Geun Lee [1], Takuya Tsutsumi [2], Hiroki Sugiyama [2], Hideaki Matsuzaki [2], Jae-Hak Lee [1] and Dae-Hyun Kim [1,*]

[1] School of Electronic and Electrical Engineering, Kyungpook National University (KNU), Daegu 41566, Republic of Korea

[2] NTT Device Technology Laboratories, Atsugi-shi 243-0198, Japan

* Correspondence: dae-hyun.kim@ee.knu.ac.kr

Abstract: We present a fully analytical model and physical investigation on the source resistance (R_S) in $In_xGa_{1-x}As$ quantum-well high-electron mobility transistors based on a three-layer TLM system. The R_S model in this work was derived by solving the coupled quadratic differential equations for each current component with appropriate boundary conditions, requiring only six physical and geometrical parameters, including ohmic contact resistivity (ρ_c), barrier tunneling resistivity ($\rho_{barrier}$), sheet resistances of the cap and channel regions (R_{sh_cap} and R_{sh_ch}), side-recessed length (L_{side}) and gate-to-source length (L_{gs}). To extract each model parameter, we fabricated two different TLM structures, such as *cap-TLM* and *recessed-TLM*. The developed R_S model in this work was in excellent agreement with the R_S values measured from the two TLM devices and previously reported short-L_g HEMT devices. The findings in this work revealed that barrier tunneling resistivity already played a critical role in reducing the value of R_S in state-of-the-art HEMTs. Unless the barrier tunneling resistivity is reduced considerably, innovative engineering on the ohmic contact characteristics and gate-to-source spacing would only marginally improve the device performance.

Keywords: source resistance; TLM; $In_xGa_{1-x}As$; HEMT

Citation: Yoo, J.-H.; Lee, I.-G.; Tsutsumi, T.; Sugiyama, H.; Matsuzaki, H.; Lee, J.-H.; Kim, D.-H. Analytical and Physical Investigation on Source Resistance in $In_xGa_{1-x}As$ Quantum-Well High-Electron-Mobility Transistors. *Micromachines* **2023**, *14*, 439. https://doi.org/10.3390/mi14020439

Academic Editor: Stephen Edward Saddow

Received: 15 January 2023
Revised: 27 January 2023
Accepted: 8 February 2023
Published: 12 February 2023

1. Introduction

The evolving sixth-generation (6G) wireless communication technologies demand higher operating frequencies of approximately 300 GHz with data rates approaching 0.1 Tbps [1,2]. To meet this urgent requirement, transistor technologies must be engineered to sustain the evolution of digital communication systems, guided by Edholm's law [3]. Among various transistor technologies, indium-rich $In_xGa_{1-x}As$ quantum-well (QW) high-electron-mobility transistors (HEMTs) on InP substrates have offered the best balance of current-gain cutoff frequency (f_T) and maximum oscillation frequency (f_{max}), and the lowest noise figure characteristics in the sub-millimeter-wave region [4–8]. These transistors adopt a combination of L_g scaling down to sub-30 nm, enhancement of the channel carrier transport by incorporating the indium-rich channel design, and reduction of all parasitic components.

Among various parasitic components, it is imperative to minimize the source resistance (R_S) itself to fully benefit from the superior intrinsic performance of the $In_xGa_{1-x}As$ QW channel [9,10], demanding an analytical and physical model for the source resistance. Considering state-of-the-art $In_xGa_{1-x}As$ HEMT technologies [11–14], source and drain contacts have been created with a non-alloyed metal stack of Ti/Pt/Au with a source-to-drain spacing (L_{ds}) between 1 µm and 0.5 µm. Historically, R_S is minimized by reducing the ohmic contact resistivity (ρ_c) [15] and shrinking the gate-to-source spacing (L_{gs}) using da self-aligned gate architecture [16,17]. However, it is very challenging to reduce R_S to below 100 Ω·µm, because of the tunneling resistance component between the heavily doped

$In_{0.53}Ga_{0.47}As$ capping layer and the $In_xGa_{1-x}As$ QW channel layer. To understand the limit of R_S in HEMTs in an effort to further reduce R_S, a sophisticated and comprehensive model must be developed for R_S in state-of-the art HEMTs, rather than the simple lumped-elements-based one-layer model [18,19].

Previously, two-layer system-based R_S model was developed by Feuer [20], which was applicable to alloyed ohmic contact structures with two different contact resistances: one was associated with a heavily doped GaAs capping layer and the other with a undoped GaAs QW channel layer. In this letter, we present a fully analytical and physical model for R_S in advanced HEMTs, requiring only six physical and geometrical parameters. The model considers three different regions: (i) a one-layer transmission-line model (TLM) for the side-recess region, (ii) an analytical TLM for the access region and (iii) an analytical three-layer TLM for the source electrode region, to accurately predict a value of R_S in a given HEMT structure and identify dominant components to further minimize R_S. To do so, we proposed and fabricated two different types of TLM structures to experimentally extract each component of R_S. The analytical model proposed in this work is in excellent agreement with the measured values of R_S from the fabricated *r-TLMs*, as well as recently reported advanced HEMTs. Most importantly, findings in this work reveal that the $\rho_{barrier}$ is a bottleneck for further reductions of R_S in advanced HEMTs.

2. Analytical Model for R_S

Figure 1a–c show the cross-sectional schematic and TEM images of advanced $In_xGa_{1-x}As$ QW HEMTs on an InP substrate [4]. They adopt non-alloyed S/D ohmic contacts such as a metal stack of Ti/Pt/Au with contact resistance (R_C) values between 10 Ω·µm and 20 Ω·µm. Carrier transfer from the cap to channel replies on a tunneling mechanism via an $In_{0.52}Al_{0.48}As$ barrier layer. To model R_S, a comprehensive transport mechanism from the source ohmic electrode to the $In_xGa_{1-x}As$ QW channel via the $In_{0.53}Ga_{0.47}As$ cap and $In_{0.52}Al_{0.48}As$ barrier layers must be considered in a distributed manner.

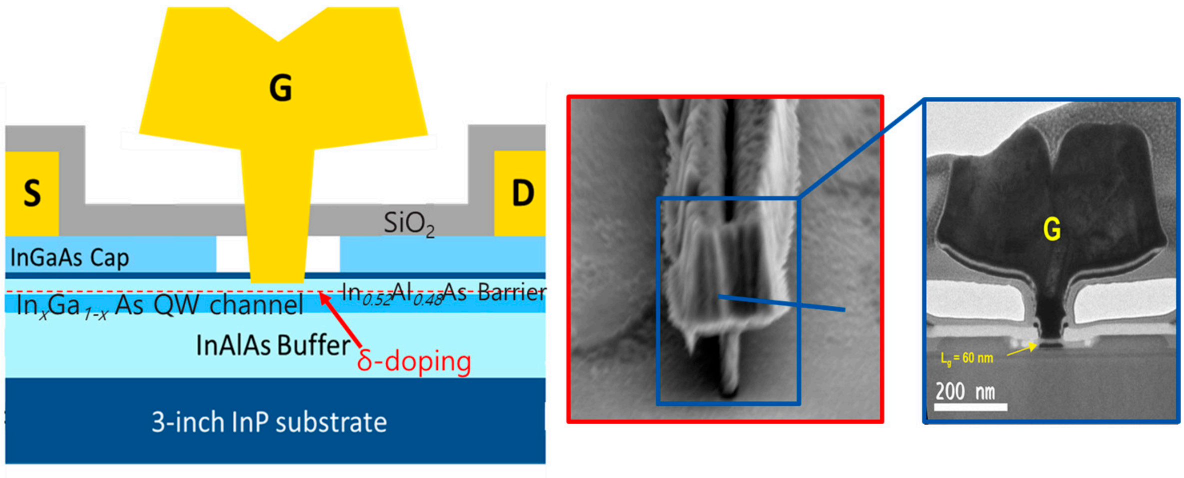

(**a**) (**b**)

Figure 1. (**a**) Cross-sectional schematic, and (**b**) TEM images of advanced $In_xGa_{1-x}As$ QW HEMTs [4].

Figure 2a illustrates a complete distributed equivalent circuit model for R_S, comprising three regions. One is the source ohmic electrode region (Region-I), where the electrons are injected from the ohmic metal to the $In_{0.53}Ga_{0.47}As$ cap and then to the $In_xGa_{1-x}As$ QW channel through the $In_{0.52}Al_{0.48}As$ barrier, which is governed by a three-layer TLM system. Another is the source access region (Region-II), where the electron transfer mechanism is governed by a cap-to-channel two-layer TLM system with transfer length ($L_{T\_barrier}$) given by $\sqrt{\rho_{barrier}/\left(R_{sh\_ch}+R_{sh\_cap}\right)}$. The other is the side-recessed region (Region-III), where a simple one-layer model works. In comparison, lumped-elements based one-layer model is shown in Figure 2c [18,19].

Next, let us derive a fully analytical and physical expression for R_S. Given the coordinate system in Figure 3a, R_S can be determined by $V_{ch}(x = -L_{gs})/I_O$ from Ohm's law, and then the problem is how to express each current component as a function of x such as $I_{ch}(x)$, $I_{cap}(x)$, and $I_{met}(x)$. In a given segment as highlighted in Figure 3b, we can define a differential contact conductance as $dg_c = (W_g/\rho_c)\,dx$, a differential barrier conductance as $dg_{barrier} = (W_g/\rho_{barrier})\,dx$, a differential lateral cap resistance as $dr_{s\_cap} = (R_{sh\_cap}/W_g)\,dx$ and a differential lateral channel resistance as $dr_{s\_ch} = (R_{sh\_ch}/W_g)\,dx$. At location x, Kirchhoff's current and voltage laws yield, respectively

$$\frac{d^2 I_{met}(x)}{dx^2} = \left[R_{met}\cdot I_{met}(x) - R_{sh\_ch}\cdot I_{cap}(x)\right]\rho_c^{-1} \tag{1}$$

$$\frac{d^2 I_{ch}(x)}{dx^2} = \left[R_{sh\_ch}\cdot I_{ch}(x) - R_{sh\_cap}\cdot I_{cap}(x)\right]\rho_{barrier}^{-1} \tag{2}$$

$$I_{cap} = I_O - I_{met} - I_{ch} \tag{3}$$

These are coupled quadratic differential equations for three current components ($I_{ch}(x)$, $I_{cap}(x)$ and $I_{met}(x)$). From the general solution for these differential equations with existing six boundary conditions (listed in Table 1), we obtain an analytical expression for $I_{ch}(x)$, $I_{cap}(x)$, and $I_{met}(x)$ for both regions, as written in Table 1. The expression for $V_{ch}(x = -L_{gs})$ can then be derived. Although there are several ways to express $V_{ch}(x = -L_{gs})$, it is useful to focus on the total voltage drop across the $In_xGa_{1-x}As$ QW channel from $x = -L_{gs}$ to $x = \infty$ in this work. From this,

$$V_{ch}(x = -L_{gs}) = \int I_{ch}(x)\cdot dr_{S\_ch}\,dx \tag{4}$$

The source resistance, defined as $V_{ch}(x = 0)/I_O$, is

$$R_S = \frac{V_{ch}(x = -L_{gs})}{I_O} = \frac{R_{sh\_ch}}{W_g I_O}\int_{-L_{gs}}^{\infty} I_{ch}(x)dx \tag{5}$$

$$\begin{aligned} R_S\cdot W_g = [&\frac{\sqrt{2}\cdot C_1\cdot\sqrt{\rho_C\cdot\rho_{barrier}}}{\rho_C\cdot\left(R_{sh\_ch}+R_{sh\_cap}\right)+\rho_{barrier}\cdot R_{sh\_cap}-\eta} + \frac{\sqrt{2}\cdot C_1\cdot\sqrt{\rho_C\cdot\rho_{barrier}}}{\rho_C\cdot\left(R_{sh\_ch}+R_{sh\_cap}\right)+\rho_{barrier}\cdot R_{sh\_cap}+\eta} \\ &+\frac{(C_3-C_4)\cdot\left(1-e^{-L_{gs}/L_{T\_barrier}}\right)}{L_{T\_barrier}} + \frac{R_{sh\_cap}\cdot L_{gs}}{\rho_{barrier}\cdot L_{T\_barrier}{}^2}] + R_{sh\_ch}\cdot L_{side} \end{aligned} \tag{6}$$

$$\eta = \sqrt{\rho_c{}^2(R_{sh\_ch}{}^2 + R_{sh\_cap}{}^2) + 2R_{sh\_ch}\,R_{sh\_cap}\rho_c(\rho_c - \rho_{barrier}) + R_{sh\_cap}{}^2\rho_{barrier}(2\rho_c + \rho_{barrier})} \tag{7}$$

$$L_{T\_barrier} = \sqrt{\frac{\rho_{barrier}}{R_{sh\_ch} + R_{sh\_cap}}} \tag{8}$$

Overall, R_S depends on the ohmic contact resistivity, the sheet resistances of the cap and QW channel layers, the barrier tunneling resistivity, and the length of the gate-to-source region and side-recessed regions.

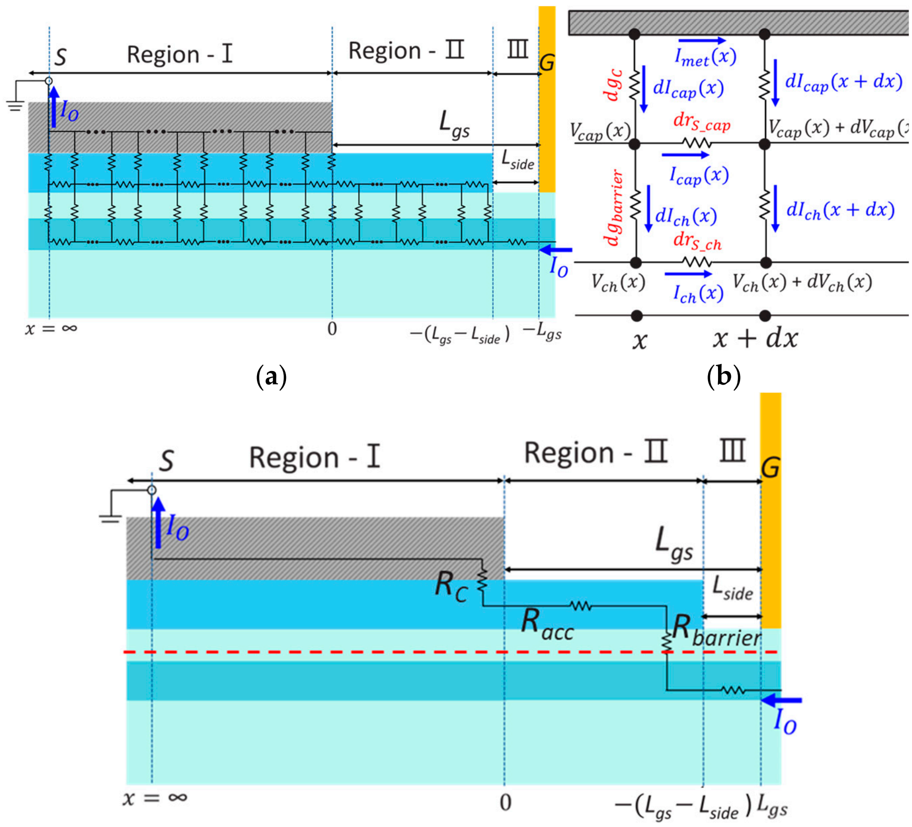

Figure 2. (**a**) Equivalent circuit model of the source structure in the advanced HEMTs, (**b**) differential segment from x to $x + dx$, and (**c**) lumped-elements based one-layer model.

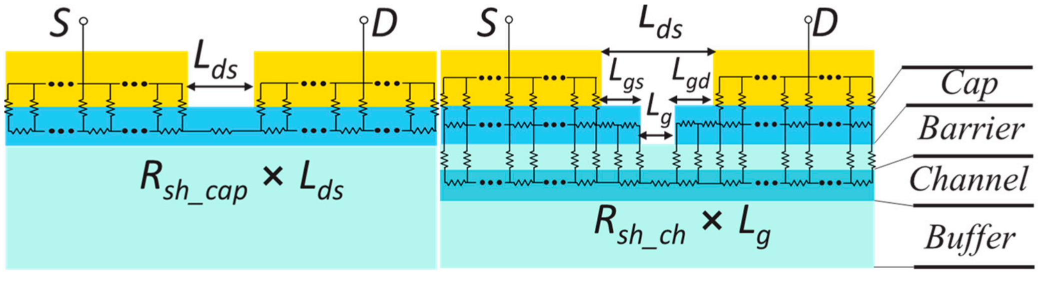

Figure 3. Cross-sectional schematic of *cap-TLM* (**a**) and recessed-TLM (*r-TLM*) (**b**).

Table 1. Six boundary conditions, the general solution for three current components, and their corresponding eigenvalues and eigenvectors.

BCs	$I_{ch} = I_O$ for $x = -L_{gs}$ $I_{cap}(x = 0^-) = I_{cap}(x = 0^+)$	$I_{met} = 0$ for $-L_{gs} < x < 0$ $I_{ch}(x = 0^-) = I_{ch}(0^+)$	$I_{met} = I_O$ for $x = \infty$ $\frac{dI_{ch}(x=0^-)}{dx} = -\frac{dI_{ch}(x=0^+)}{dx}$
Region-I	$\begin{bmatrix} I_{met} \\ I_{ch} \end{bmatrix} = \begin{bmatrix} v_{11} \\ v_{12} \end{bmatrix} C_1 exp\left(-\sqrt{\lambda_1}x\right) + \begin{bmatrix} v_{21} \\ v_{22} \end{bmatrix} C_2 exp\left(-\sqrt{\lambda_2}x\right) + \begin{bmatrix} I_O \\ 0 \end{bmatrix}$ $I_{cap} = I_O - I_{met} - I_{ch}$	Region-II	$I_{cap} = C_3 exp\left(\frac{-x}{L_{T\_barrier}}\right) + C_4 exp\left(\frac{x}{L_{T\_barrier}}\right) + \frac{R_{sh\_ch}}{R_{sh\_cap}+R_{sh\_ch}} I_O$ $I_{ch} = I_O - I_{cap}$
	$-\lambda_1$ & λ_2 are eigenvalues of $A = \begin{bmatrix} \left(\frac{R_{sh\_cap}}{\rho c}\right) & \left(\frac{R_{sh\_cap}}{\rho c}\right) \\ \left(\frac{R_{sh\_cap}}{\rho_{barrier}}\right) & \left(\frac{R_{sh\_cap}+R_{sh\_cap}}{\rho_{barrier}}\right) \end{bmatrix}$ $-\begin{bmatrix} v_{11} \\ v_{12} \end{bmatrix}$ & $\begin{bmatrix} v_{21} \\ v_{22} \end{bmatrix}$ are their corresponding eigenvectors	$\begin{bmatrix} C_1 \\ C_2 \\ C_3 \\ C_4 \end{bmatrix} = \begin{bmatrix} 0 & 0 & exp\left(\frac{L_{gs}}{L_{T\_barrier}}\right) & exp\left(\frac{-L_{gs}}{L_{T\_barrier}}\right) \\ v_{12} & v_{22} & 1 & 1 \\ v_{11} & v_{21} & 0 & 0 \\ -\sqrt{\lambda_1}v_{12} & -\sqrt{\lambda_2}v_{22} & -\frac{1}{L_{T\_barrier}} & \frac{1}{L_{T\_barrier}} \end{bmatrix}^{-I} \begin{bmatrix} -\frac{R_{sh\_ch} \times I_O}{R_{sh\_cap}+R_{sh\_ch}} \\ I_O\left(1 - \frac{R_{sh\_ch}}{R_{sh\_cap}+R_{sh\_ch}}\right) \\ -I_O \\ 0 \end{bmatrix}$	

3. Experimental Results and Discussion

Two types of TLM structures were fabricated, as shown in Figure 3: the cap-only TLM structure (*cap-TLM*, (a)) to evaluate the contact characteristics of the non-alloyed ohmic metal stack, and the recessed TLM structure (*r-TLM*, (b)) which is identical to the real device without a Schottky gate electrode. Details on the epitaxial layer design and device processing were reported in our previous paper [4]. All device processing was conducted on a full 3-inch wafer with an i-line stepper to ensure fine alignment accuracy within 0.05 μm. In the *r-TLM*, we varied L_g from 40 μm to 0.5 μm and L_{gs} from 10 μm to 0.2 μm. In this way, the split of L_g yielded the sheet resistance of the QW channel (R_{sh_ch}) from the linear dependence, and the source resistance (R_S) from the y-intercept at a given L_{gs}. Lastly, we investigated the dependence of R_S on L_{gs} in detail.

Figure 4 plots the measured total resistance (R_T) against L_{ds}, which corresponds to the length between the edge of source and the edge of drain. for the fabricated *cap-TLM* structures. This yielded values of R_{sh_cap} = 131 Ω/sq, R_C = 32 Ω·μm, L_{T_cap} = 0.34 μm and ρ_c = 15 Ω·μm^2, with an excellent correlation coefficient of 0.99999. Figure 5a plots the measured R_T against L_g for the *r-TLM* structures with various dimensions of L_{gs} from 10 μm to 0.2 μm. When L_g was long enough, each *r-TLM* device yielded approximately the same slope for all L_{gs} with excellent correlation coefficient. This is plotted in Figure 5b with averaged R_{sh_ch} = 145 Ω/sq and excellent $\Delta(R_{sh\_ch})$ = 1.56 Ω/sq, confirming that the $In_{0.8}Ga_{0.2}As$ QW channel sheet resistance was independent of L_{gs}. Because we designed the symmetrical L_{gs} and L_{gd}, half of the y-intercept from Figure 6a corresponded exactly to R_S. In analyzing *r-TLM* structures with various L_{gs}, values of the correlation coefficient were also greater than 0.999, increasing the credibility of the overall TLM analysis.

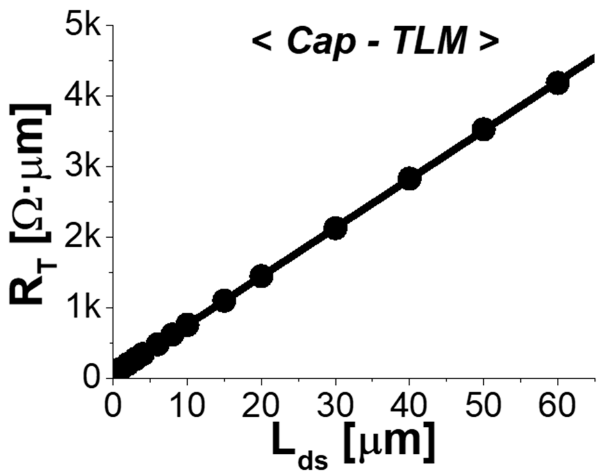

Figure 4. Measured total resistance (R_T) as a function of L_{ds} for *cap-TLM*.

Figure 6 plots the measured R_S (filled symbols) from the *r-TLM* analysis against L_{gs}, as well as the projected R_S (line) from Equation (5) with the model parameters of $\rho_{barrier}$ = 91 Ω·μm^2 and others directly from the *cap-TLMs* and *r-TLMs*. Additionally, the open symbols in Figure 6 came from the R_S extracted directly from the reported HEMTs [4] using the gate-current injection technique [21]. There are two points to identify in Figure 6. First, all of the measured R_S characteristics were explained by the modeled R_S. Second, R_S was linearly proportional to L_{gs} for L_{gs} > 1 μm, where its slope was 69 Ω/sq. Interestingly, this was similar to the parallel connection of R_{sh_cap} and R_{sh_ch}. However, this linear dependence of R_S on L_{gs} was no longer valid for L_{gs} < 1 μm and, most importantly, the measured R_S eventually saturated to approximately 123 Ω·μm even with L_{gs} approaching 0. Our model clearly indicated that this was because of the barrier tunneling resistivity. The saturation of R_S in L_{gs} = 0 was because the necessary lateral length for the cap-to-channel tunneling was supplied by its equivalent transfer length from the leading edge of the source metal contact ($-L_{T\_barrier} < x < 0$) in Region-I.

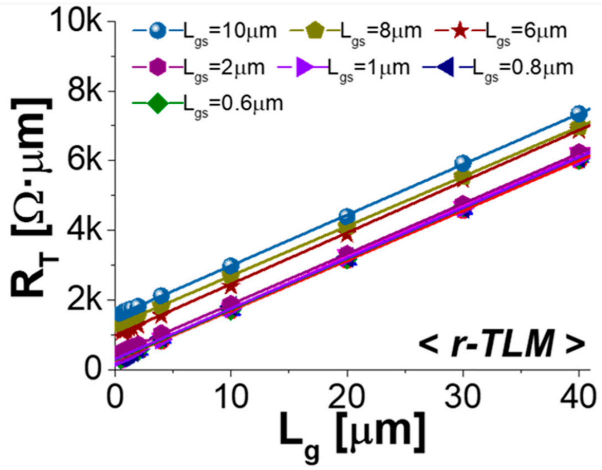

(**a**)

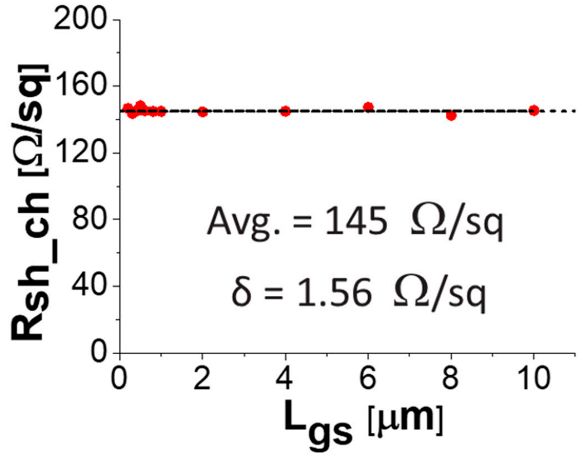

(**b**)

Figure 5. (**a**) Measured total resistance (R_T) as a function of L_g for *r-TLM* with various dimensions of L_{gs} from 10 μm to 0.2 μm, and (**b**) the extracted sheet resistance of the $In_xGa_{1-x}As$ QW channel (R_{sh_ch}) as a function of L_{gs}.

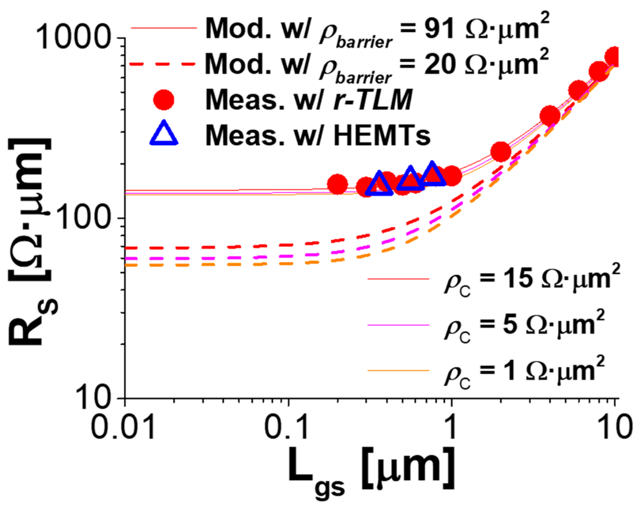

Figure 6. Comparison of the modeled and measured R_S against L_{gs} in the *log-log* scale.

Finally, let us discuss how to further reduce R_S with the R_S model proposed in this work. The three solid lines in Figure 6 are the model projections of R_S with the ohmic contact resistivity improve from 15 $\Omega \cdot \mu m^2$ (present) to 1 $\Omega \cdot \mu m^2$. Surprisingly, R_S would not be minimized even with a significant reduction in ρ_c and L_{gs} because of the $\rho_{barrier}$. Alternatively, the three dashed lines in Figure 6 are from the same model projection, but with $\rho_{barrier}$ = 20 $\Omega \cdot \mu m^2$. Note that a reduction in the $\rho_{barrier}$ is important; in consequence, the projected R_S would be significantly scaled down to 70 $\Omega \cdot \mu m$ and below. Under this circumstance, R_S could then be further reduced by the improved ohmic contact characteristics and the reduction of L_{gs}.

4. Conclusions

A fully analytical and physical investigation on R_S in advanced $In_xGa_{1-x}As$ QW HEMTs was carried out with a three-layer TLM system. Analytical solutions to the three current components (source metal, cap, and channel) along the selected coordinate system with appropriate boundary conditions were produced. The proposed R_S model in this work required only six physical and geometrical parameters (ρ_c, $\rho_{barrier}$, R_{sh_cap}, R_{sh_ch}, L_{side} and L_{gs}), yielding excellent agreement with the R_S values measured from the two TLM devices and previously reported $In_xGa_{1-x}As$ QW HEMTs. The developed model in this work was capable of explaining the saturation behavior of R_S for $L_{gs} < 1$ μm, which was due to the $\rho_{barrier}$. Therefore, one must pay a more careful attention to cut down the $\rho_{barrier}$ to further minimize R_S in future HEMTs.

Author Contributions: Conceptualization, J.-H.Y. and D.-H.K.; device fabrication, J.-H.Y., I.-G.L. and D.-H.K.; formal analysis, J.-H.Y., T.T., H.S., H.M. and D.-H.K.; investigation, J.-H.Y., J.-H.L. and D.-H.K.; resources, J.-H.Y., J.-H.L. and D.-H.K.; writing—original draft preparation, J.-H.Y.; writing—review and editing, I.-G.L.; supervision, J.-H.L. and D.-H.K.; funding acquisition, D.-H.K. All authors have read and agreed to the published version of the manuscript.

Funding: This research was supported by the Civil-Military Technology Cooperation program (No. 19-CM-BD-05).

Data Availability Statement: The data presented in this study are available on request from the corresponding author.

Conflicts of Interest: The authors declare no conflict of interest.

References

1. Cahoon, N.; Srinivasan, P.; Guarin, F. 6G Roadmap for Semiconductor Technologies: Challenges and Advances. In Proceedings of the IEEE International Reliability Physics Symposium, Dallas, TX, USA, 27–31 March 2022.
2. Ikram, M.; Sultan, K.; Lateef, M.F.; Alqadami, A.S.M. A Road towards 6G Communication—A Review of 5G Antennas, Arrays, and Wearable Devices. *Electronics* **2022**, *11*, 169. [CrossRef]
3. Cherry, S. Edholm's law of bandwidth. *IEEE Spectr.* **2004**, *41*, 7. [CrossRef]
4. Jo, H.-B.; Yun, S.-W.; Kim, J.G.; Yun, D.-Y.; Lee, I.G.; Kim, D.-H.; Kim, T.-W.; Kim, S.-K.; Yun, J.; Kim, T.; et al. L_g = 19 nm $In_{0.8}Ga_{0.2}As$ composite channel HEMTs with f_T = 738 GHz and f_{max} = 492 GHz. In Proceedings of the IEEE International Electron Devices Meeting, San Francisco, CA, USA, 12–18 December 2020.
5. Cooke, C.M.; Leong, K.M.K.H.; Zamora, A.; Gorospe, B.S.; Mei, X.B.; Kangaslahti, P.; Schlecht, E.; Ogut, M.; Goncharenko, Y.; Reising, S.C.; et al. A 670 GHz Integrated InP HEMT Direct-Detection Receiver for the Tropospheric Water and Cloud Ice Instrument. *IEEE Trans. Electron Devices* **2021**, *11*, 566. [CrossRef]
6. Leuther, A.; Koch, S.; Tessmann, A.; Kallfass, I.; Merkle, T.; Massler, H.; Loesch, R.; Schlechtweg, M.; Saito, S.; Ambacher, O. 20 NM metamorphic HEMT WITH 660 GHZ FT. In Proceedings of the International Conference on Indium Phosphide and Related Materials, Berlin/Heidelberg, Germany, 22–26 May 2011.
7. Yun, S.-W.; Jo, H.-B.; Yoo, J.-H.; Park, W.-S.; Jeong, H.-S.; Choi, S.-M.; Kim, H.-J.; George, S.; Beak, J.-M.; Lee, I.-G.; et al. InxGa1−xAs quantum-well high-electron-mobility transistors with a record combination of fT and fmax: From the mobility relevant to ballistic transport regimes. In Proceedings of the IEEE Electron Devices Meeting, San Francisco, CA, USA, 11–16 December 2021.
8. Takahashi, T.; Kawano, Y.; Makiyama, K.; Shiba, S.; Sato, M.; Nakasha, Y.; Hara, N. Enhancement of fmax to 910 GHz by Adopting Asymmetric Gate Recess and Double-Side-Doped Structure in 75-nm-Gate InAlAs/InGaAs HEMTs. *IEEE Trans. Electron Devices* **2017**, *64*, 89–95. [CrossRef]

9. Tasker, P.J.; Hughes, B. Importance of source and drain resistance to the maximum f/sub T/ of millimeter-wave MODFETs. *IEEE Electron. Device Lett.* **1989**, *10*, 291–293. [CrossRef]
10. Shinohara, K.; Yamashita, Y.; Endoh, A.; Watanabe, I.; Hikosaka, K.; Matsui, T.; Mimura, T.; Hiyamizu, S. 547-GHz f/sub t/ In/sub 0.7/Ga/sub 0.3/As-In/sub 0.52/Al/sub 0.48/As HEMTs with reduced source and drain resistance. *IEEE Electron. Device Lett.* **2004**, *25*, 241–243. [CrossRef]
11. Chang, E.-Y.; Kuo, C.-I.; Hsu, H.-T.; Chiang, C.-Y.; Miyamoto, Y. InAs Thin-Channel High-Electron-Mobility Transistors with Very High Current-Gain Cutoff Frequency for Emerging Submillimeter-Wave Applications. *Appl. Phys. Express* **2013**, *6*, 034001. [CrossRef]
12. Jo, H.-B.; Yun, S.-W.; Kim, J.-G.; Baek, J.-M.; Lee, I.-G.; Kim, D.-H.; Kim, T.-W.; Kim, S.-K.; Yun, J.; Kim, T.; et al. Sub-30-nm In0.8Ga0.2As Composite-Channel High-Electron-Mobility Transistors With Record High-Frequency Characteristics. *IEEE Trans. Electron. Devices* **2021**, *68*, 2010–2016. [CrossRef]
13. Mei, X.; Yoshida, W.; Lange, M.; Lee, J.; Zhou, J.; Liu, P.-H.; Leong, K.; Zamora, A.; Padilla, J.; Sarkozy, S.; et al. First Demonstration of Amplification at 1 THz Using 25-nm InP High Electron Mobility Transistor Process. *IEEE Electron. Device Lett.* **2015**, *36*, 327–329. [CrossRef]
14. Yun, D.-Y.; Jo, H.-B.; Son, S.-W.; Baek, J.-M.; Lee, J.-H.; Kim, T.-W.; Kim, D.-H.; Tsutsumi, T.; Sugiyama, H.; Matsuzaki, H. Lg=87 nm InAlAs/InGaAs High-Electron- Mobility Transistors With a g m_max of 3 S/mm and fT of 559 GHz. *IEEE Electron. Device Lett.* **2018**, *39*, 1640–1643.
15. Crook, A.M.; Lind, E.; Griffith, A.; Rodwell, W.M.J. Low resistance, nonalloyed Ohmic contacts to InGaAs. *Appl. Phys. Lett.* **2007**, *91*, 192114. [CrossRef]
16. Waldron, N.; Kim, D.-H.; del Alamo, J.A. A self-aligned InGaAs HEMT architecture for logic applications. *IEEE Trans. Electron. Devices* **2010**, *57*, 297–304. [CrossRef]
17. Moran, D.A.J.; McLelland, H.; Elgaid, K.; Whyte, G.; Stanley, C.R.; Thayne, I. 50-nm Self-Aligned and "Standard" T-gate InP pHEMT Comparison: The Influence of Parasitics on Performance at the 50-nm Node. *IEEE Trans. Electron. Devices* **2006**, *53*, 2920–2925. [CrossRef]
18. Takahashi, T.; Sato, M.; Makiyama, K.; Hirose, T.; Hara, N. InAlAs/InGaAs HEMTs with Minumum Noise Figure of 1.0dB AT 94 GHz. In Proceedings of the IEEE 19th International Conference on Indium Phosphide & Related Materials, Matsue, Japan, 14–18 May 2007.
19. Jeong, J.; Kim, S.K.; Kim, J.M.; Geum, D.-M.; Lee, J.; Park, S.-Y.; Kim, S. 3D stackable cryogenic InGaAs HEMTs for heterogeneous and monolithic 3D intergrated highly scalable quantum computing systems. In Proceedings of the IEEE Symposium on VLSI Technology and Circuits, Honolulu, HI, USA, 12–17 June 2022.
20. Feuer, M.D. Two-layer model for source resistance in selectively doped heterojunction transistors. *IEEE Trans. Electron. Devices* **1985**, *32*, 7–11. [CrossRef]
21. Azzam, W.J.; Del Alamo, J.A. An all-electrical floating-gate transmission line model technique for measuring source resistance in heterostructure field-effect transistors. *IEEE Trans. Electron. Devices* **1990**, *37*, 2105–2107. [CrossRef]